ROYAL SOCIETY
OF CHEMISTRY

PAPER

Check for updates

Regulating the metal nodes of 1D conjugated coordination polymers for enhancing the performance of sodium-ion batteries†‡

Kun Fan, Chenyang Zhang, Yuan Chen, Guoqun Zhang, Yanchao Wu, Jincheng Zou and Chengliang Wang ✦ *

Conjugated coordination polymers (CCPs) have attracted extensive attention for energy storage in the past few years. However, the rational design and controllable synthesis of CCPs remain challenging, which prevents gaining insight into the relationship between structure and electrochemical performance and limits the potential applications of CCPs. Herein, 2,5-dihydroxy-1,4-benzoquinone (H_2DHBQ) is selected to construct one dimensional CCPs **M-DHBQ** with different metal ions, including Ni^{2+}, Mn^{2+} and Zn^{2+}. Comprehensive characterizations indicated that the high capacity of **Ni-DHBQ** was due to the redox reactions of both ligands and non-innocent Ni^{2+} ions. On the other hand, the sodium storage of **Mn-** and **Zn-DHBQ** involved the redox reactions of only ligands. These results highlighted the importance of the rational choice of metal ions for high capacity and cycle stability, and deepen our understanding on CCPs for further designing high performance energy storage devices.

Introduction

Electroactive organic compounds have received great attention for batteries, due to their fascinating features of flexibility, high theoretical capacities, structural diversity, renewability and low cost.[1–3] However, some intrinsic problems, such as undesirable dissolution in organic electrolytes and low electrical conductivity, resulting in poor cycle stability as well as limited rate capability, have still restricted the widespread use of organic materials in energy storage devices.[4] Although tremendous strategies have been proposed to address these problems, such as salification, polymerization and manipulation of conductive additives, binders, electrolytes and separators, normally they could only solve part of the challenges.[5,6]

Recently, conjugated coordination polymers (CCPs), which combine electroactive organic ligands with metal ions, have attracted extensive attention.[7–10] Owing to the hybridization between the π orbitals of conjugated ligands and the d orbitals of transition metals, CCPs possess a lot of merits for high-performance batteries.[11–15] The π–d systems will effectively promote the delocalization of electrons and significantly enhance the electrical conductivity and stability, which benefit

the long-term cyclability and the rate performance of batteries.[16–19] There is no doubt that the electrochemical behaviours of CCPs could be enhanced by the judicious choice of organic ligands and metals to ensure high-performance metal-ion batteries.[20–26] However, due to the complicated synthesis process, including *in situ* deprotonation, oxidation, and coordination, the rational design and controllable synthesis of CCPs remain challenging, which prevents the deep understanding of charge storage mechanisms and gaining insight into the relationship between the structure and the electrochemical performance and limits the potential applications of CCPs.[27–31]

Herein, 2,5-dihydroxy-1,4-benzoquinone (H_2DHBQ), which is known as a bis-bidentate ligand with a π-electron system,[32–34] was selected as the ligand to form one dimensional conjugated coordination polymers with different metal nodes (**M-DHBQ**, M = Ni, Mn and Zn) for sodium-ion batteries (SIBs). Comprehensive characterizations revealed that the sodium storage of **Mn-** and **Zn-DHBQ** involved the redox reactions of only ligands, while **Ni-DHBQ** involved the redox reactions of both ligands and non-innocent Ni^{2+} ions. Benefiting from the redox active quinone groups as well as metal ions, **Ni-DHBQ** delivered a high reversible capacity of around 302.3 mA h g^{-1} at 0.1 A g^{-1} after 150 cycles and superior rate performance ($\sim$267 mA h g^{-1} at 2 A g^{-1}). These results highlighted the importance of the rational choice of metal ions for high capacity and cycle stability, and deepen our understanding on CCPs for further designing high performance SIBs.

School of Optical and Electronic Information, Wuhan National Laboratory for Optoelectronics (WNLO), Huazhong University of Science and Technology, Wuhan 430074, China. E-mail: clwang@hust.edu.cn

Results and discussion

Synthesis and characterization

One dimensional CCPs (**M-DHBQ**, M = Mn, Zn, and Ni) were synthesized by the reaction of DHBQ and the corresponding metal salt in H_2O at 100 °C.[35] As shown in scanning electron microscopy (SEM) images, **Mn-DHBQ** exhibited a regular cuboid shape with size in the micron range, while **Zn-DHBQ** and **Ni-DHBQ** showed regular rod-like morphologies with smaller size (Fig. 1a–c). The uniform distribution of elements in bulk samples was confirmed by energy-dispersive X-ray spectroscopy (EDS) (Fig. S1–S3, ESI‡). FTIR spectroscopy was performed to characterize the chemical composition. Compared with the free ligand, the disappearance of the sharp absorption peak at about 3300 cm^{-1} and three absorption peaks at around 1200 cm^{-1} indicated the deprotonation of OH groups and the coordination of O with metal ions (Fig. S4, ESI‡).[36] The C=O absorption shifted to low frequencies at 1530 cm^{-1}, which was similar to the related materials containing the dianionic DHBQ^{2-} ligand.[37,38] Moreover, the C–O absorption shifted to high frequencies at 1263 cm^{-1}. These results indicated the efficient electron delocalization after coordination. Altogether, they clearly demonstrated that metal centres were successfully coordinated with the bidentate ligands. On the other hand, the broad absorption peak at about 3300 cm^{-1}, which represents O–H stretching vibrations but is different from the sharp peak in the free ligand, probably indicated the presence of coordination water.[39]

The powder X-ray diffraction patterns (PXRD) of **M-DHBQ** showed quite similar diffraction peaks, indicating that the three CCPs had similar packing motifs (Fig. S5, ESI‡).

Moreover, the obtained **Mn-DHBQ** matched well with the simulated patterns of the previously reported structure,[33] which contained two coordination water molecules above and beneath the plane of CCP molecules, respectively. The packing motifs of **Zn-** and **Ni-DHBQ** were hence simulated accordingly.[34] These results confirmed the high crystallinity of as-synthesized samples and proved the presence of coordination water molecules in the crystal structures. Fig. 1e and f show an example lattice structure of **Ni-DHBQ**, which can be further confirmed by Rietveld refinement with low residual values (R_{wp} = 5.11%, R_p = 4.08%) (Fig. 1d). As illustrated in Fig. 1e, the tetra-substituted benzene linkers with D_{2h} symmetry assembled into a 1D π–d conjugated polymer chain, in which the metal ions were connected by two bidentate ligands forming a planar polymer chain and two water molecules were located above and beneath the plane, resulting in a hexa-coordination and an octahedral geometry. The adjacent chains exhibit a staggered parallel packing motif, and are stabilized by hydrogen bonds between axial coordinated solvent molecules (Fig. 1f).

The thermogravimetric profiles of **M-DHBQ** also exhibited similar behaviours for the three CCPs. All of them showed a weight loss of about 16% in the temperature range from 100 to 230 °C, which could be assigned to the release of two coordination water molecules and coincided well with the abovementioned analyses (Fig. S6, ESI‡). Among them, the slightly lower temperature for water loss of **Mn-DHBQ** and **Zn-DHBQ** than **Ni-DHBQ** is in accordance with the lower Lewis acidity of manganese and zinc than the nickel ion.[34] However, benefiting from the increased stabilization of the metal–oxygen bonds
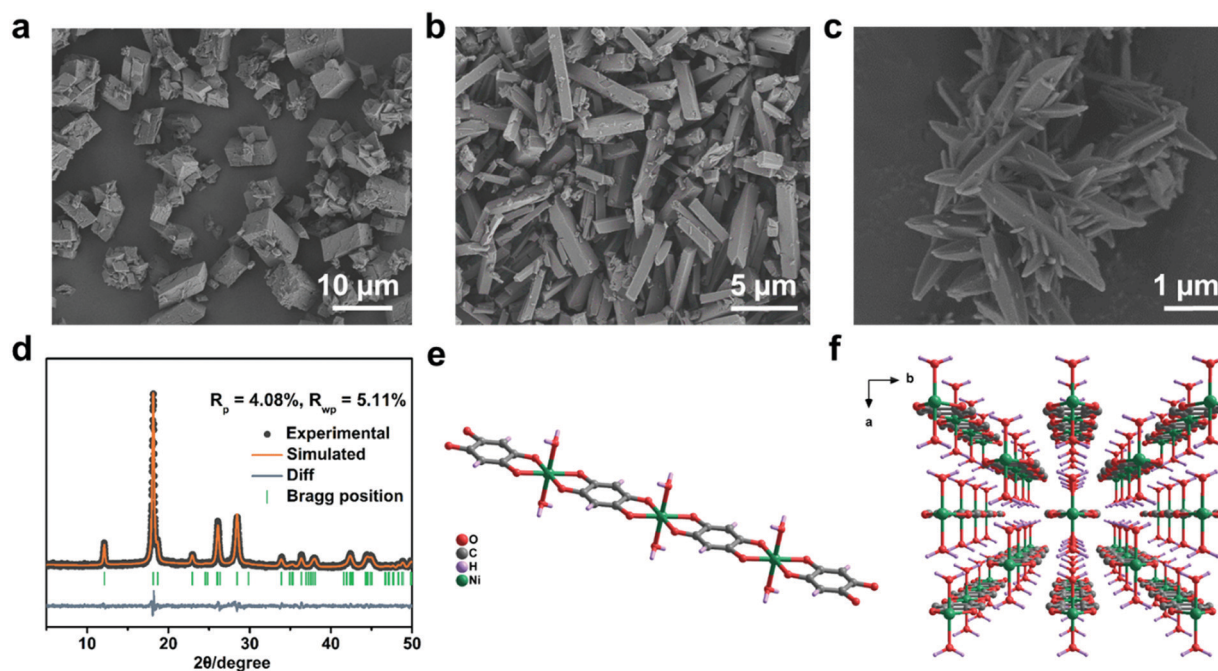

Fig. 1 (a)–(c) SEM images of **Mn-DHBQ**, **Zn-DHBQ** and **Ni-DHBQ**. (d) XRD patterns of **Ni-DHBQ**. Pawley-refined XRD patterns (simulated) are also shown for comparison. (e) The 1D chain structure of **Ni-DHBQ** and (f) perspective view of **Ni-DHBQ** along the c axis.

This journal is © The Royal Society of Chemistry 2022

J. Mater. Chem. C, 2022, **10**, 2592–2599 | **2593**

through π-electron delocalization, all three samples showed high thermal stability afterwards.[40] The decomposition temperatures for the three CCPs were higher than 350 °C, probably corresponding to the damage of the coordination structures. The high stability also indicated the high quality and high crystallinity of the obtained CCPs.

Electrochemical performance of M-DHBQ

In order to study the electrochemical performance of the materials, cyclic voltammetry (CV) curves of the three materials within a cutoff voltage window of 0.01–2.5 V (*vs.* Na$^+$/Na) were investigated at a current density of 0.5 mV s^{-1}. During the first negative sweep, **Mn-DHBQ** showed a broad reduction peak located at 1.49 V (Fig. 2a). In the subsequent positive sweeps, two broad peaks at around 1.63 and 1.90 V could be observed and were ascribed to the oxidation of the electrodes. However, after ten cycles, the broad redox peaks became very weak gradually and were split into two peaks centered at 1.24 and 1.17 V for reduction and 1.58 and 1.29 V for oxidation. The total electron transfer number of the two distinct peaks calculated from the integral area was two, which can be ascribed to the two-electron transfer reaction of the two carbonyl groups (C=O), accompanying the intercalation/extraction of sodium ions.[41,42] In the subsequent cycles, the CV curves were well overlapped, indicating the high reversibility of **Mn-DHBQ**. **Zn-DHBQ** showed quite a similar activation process and almost the same potentials of the two sharp redox peaks after activation (1.23, 1.17 for reduction and 1.61, 1.31 V for oxidation), although the initial broad redox peaks remained for more charge/discharge cycles (Fig. 2b). These results indicated the similar electrochemical performance of **Mn-DHBQ** and **Zn-DHBQ**, which probably involved the two-electron transfer process due to the reversible redox reaction of the ligands (C=O bonds). The activation process of the two materials also implied their high crystallinity, and the longer activation

process of **Zn-DHBQ** than that of **Mn-DHBQ** suggested the higher crystallinity of **Zn-DHBQ** (Fig. S5, ESI‡), although the grain size of **Mn-DHBQ** was even larger.

Although the CV curves of **Ni-DHBQ** showed a similar activation process and almost the same potentials of the two pairs of sharp redox peaks after activation (1.21/1.58 V and 1.18/1.31 V) as those of **Mn-DHBQ** and **Zn-DHBQ**, the first cathodic scan of **Ni-DHBQ** was quite different from that of the other two materials (Fig. 2c). The similar activation process and almost the same potentials of the two sharp redox peaks after activation of **Ni-DHBQ** indicated that **Ni-DHBQ** at least involved similar electrochemical reactions as its counterparts, which may be related to the reversible redox reaction of the C=O groups in organic ligands. The similar sharp redox peaks of the three materials are further illustrated in Fig. 2d. In addition to the broad peak at about 1.60 V (probably splitting into two pairs of sharp redox peaks afterwards), the first cathode scan of **Ni-DHBQ** also showed one broad peak at about 0.42 V and a shoulder peak at about 0.75 V. The peak at 0.42 V probably could be attributed to the irreversible electrolyte decomposition and the formation of solid–electrolyte interphase (SEI), and it had entirely disappeared in the second scan. On the other hand, the additional broad peak at about 0.66 V after the first cycle may be related to the reduction of Ni^{2+}.[43] Although this peak became weak gradually after ten cycles, the current in this voltage range remained at a relatively high value, indicating the retained redox reactions.

Battery performance of M-DHBQ

The three materials were then tested in 2032 cells under the same conditions. The galvanostatic charge/discharge profiles of **M-DHBQ** at a current density of 0.1 A g^{-1} are shown in Fig. 3a and b and Fig. S7 (ESI‡). The charge/discharge profiles of them showed a similar activation process to their corresponding CV curves. In addition, the three materials exhibited plateaus similar to the redox peaks of the CV curves. A particular note is that the capacity contributions of **Mn-DHBQ** and **Zn-DHBQ** were mostly achieved at voltages higher than 1.0 V (plateaus at about 1.2 V), which should be involving the transformation of C=O bonds to C–O bonds.[42] After activation of 20 cycles, the **Mn-DHBQ** electrodes could deliver a discharge capacity of 261 mA h g^{-1}. After deducting the contribution of super P, the capacity contribution of **Mn-DHBQ** was about ∼191 mA h g^{-1}, which approximated the theoretical capacity (234 mA h g^{-1}) of a two-electron redox reaction per coordination unit (Fig. 3c and Fig. S8, ESI‡). However, after deducting the contribution of super P, the capacity contribution of **Zn-DHBQ** was only about ∼143 mA h g^{-1} after activation (Fig. 3c and Fig. S7, S8, ESI‡), quite less than that of the two-electron redox reaction (theoretical capacity: 225 mA h g^{-1}), which may be ascribed to the incomplete activation process and confirmed by the retained broad reduction peak in CV curves.

In contrast, **Ni-DHBQ** electrodes delivered high initial discharge/charge capacities of 777.1/539.8 mA h g^{-1} at the first cycle with low initial coulombic efficiency (CE) which should be attributed to the formation of the SEI layer.[44–46] The capacity

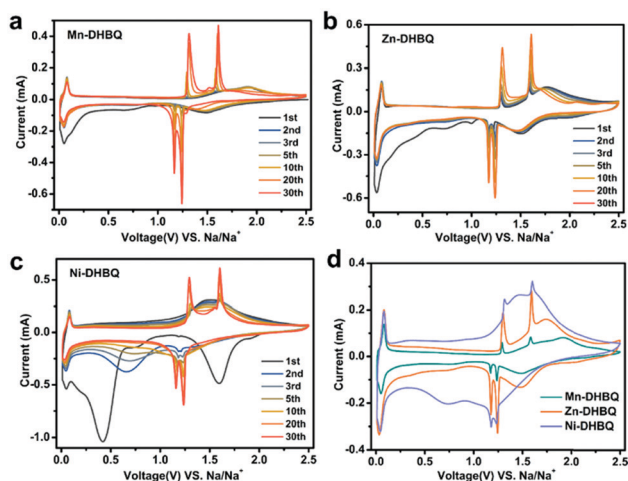**Fig. 2** CV curves of (a) **Mn-DHBQ**, (b) **Zn-DHBQ** and (c) **Ni-DHBQ** at a scan rate of 0.5 mV s^{-1} in the voltage range of 0.01–2.5 V (*vs.* Na/Na$^+$). (d) Comparison of the CV curves of **M-DHBQ** at the 5th cycle.
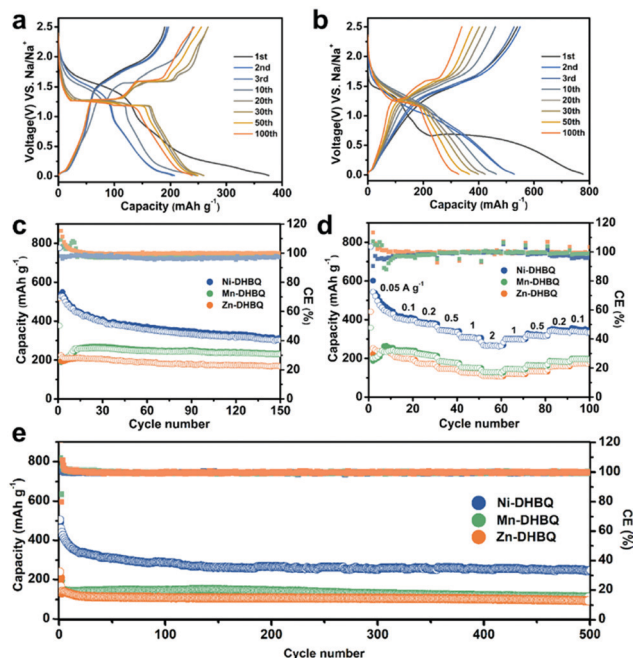
Fig. 3 Discharge–charge voltage profiles of (a) **Mn-DHBQ** and (b) **Ni-DHBQ** electrodes at a current density of 0.1 A g^{-1}. (c) Cycling performance of **M-DHBQ** electrodes at a current density of 0.1 A g^{-1}. (d) Rate capability of **M-DHBQ**. (e) Cycling performance of **M-DHBQ** electrodes at a current density of 1 A g^{-1}.

decreased gradually afterwards. Different from **Mn-DHBQ** and **Zn-DHBQ**, the capacity of **Ni-DHBQ** was about 353.4 mA h g^{-1} (Fig. 3b and Fig. S8, ESI‡), after 20 cycles and after deducting the contribution of super P, with CE approaching 98%. The capacity was slightly higher than that of a three-electron redox process for every unit (theoretical capacity of 347 mA h g^{-1}) (Fig. 2b). The capacity of **Ni-DHBQ** electrodes decreased continuously and remained at ∼302.3 mA h g^{-1} after 150 cycles (Fig. 3c). The capacity was higher than that of **Mn-DHBQ** and **Zn-DHBQ**. However, low CE and more obvious capacity fading could be observed in **Ni-DHBQ**, which was probably related to the irreversible reaction at low voltages and agreed well with the current decrease as observed in CV (which will be further discussed in the following).

The rate performance of the **M-DHBQ** anode is displayed in Fig. 2d. The **Ni-DHBQ** anode delivered an average discharge capacity of 503, 405, 380, 341, 307 and 267 mA h g^{-1} at various current densities of 50, 100, 200, 500, 1000, and 2000 mA g^{-1}, respectively. Capacity decay could also be observed (336 mA h g^{-1}) when the current density was reduced back to 100 mA g^{-1}. Nevertheless, the capacity retention (66% at 2 A g^{-1}) of **Ni-DHBQ** were still superior to those of **Mn-DHBQ** (∼55%) and **Zn-DHBQ** (∼54%) compared to the corresponding capacity at 0.1 A g^{-1} (Fig. S9–S11, ESI‡). The higher conductivity of **Ni-DHBQ** may be one of the reasons for its higher rate performance (Fig. S12, ESI‡). The long-term cycling performance of **M-DHBQ** at a higher current density of 1 A g^{-1} was further evaluated. **Ni-DHBQ** also showed a higher discharge specific capacity of ∼248.2 mA h g^{-1} after 500 cycles than **Mn-DHBQ** and **Zn-DHBQ** (Fig. 3d), although the capacity retention

of **Ni-DHBQ** was lower (53% for **Ni-DHBQ**, 67% for **Mn-DHBQ**, 55% for **Zn-DHBQ**).

Reaction kinetics of M-DHBQ

In order to further investigate the reaction kinetics of **M-DHBQ**, the CV curves at different scan rates were measured. As shown in Fig. 4a and Fig. S13, S14 (ESI‡), the shapes of all redox peaks remained the same with the increase of scan rate, suggesting the superior rate performance. Whether the process was diffusion controlled or was due to the surface capacitive effect was then analysed by using the equation $i = a\nu^b$, where i was the current and ν was the scan rate. As shown in Fig. S13 (ESI‡), the average b-value of **Mn-DHBQ** was 0.55 for the discharge/charge process, indicating a diffusion-controlled phenomenon due to the long ionic diffusion length in the large particles. For **Zn-DHBQ** with smaller particle size, the effect of the diffusion controlled process weakened (Fig. S14, ESI‡).[47] Of note, the average b-value of **Ni-DHBQ** reached 0.7, suggesting that both capacitive and diffusion-controlled processes contributed to the total capacity (Fig. S15, ESI‡). The capacitive contributions are calculated to be 63%, 68%, 74%, 80%, and 91% at the scan rates of 0.2, 0.5, 1.0, 2.0 and 5.0 mV s^{-1}, respectively (Fig. 4b and Fig. S16, ESI‡). The higher capacitive contribution at higher scan rates could be ascribed to the insufficient time for mass transfer. The comparison between **Mn-DHBQ** and **Zn-DHBQ** indicated that the higher crystallinity of **Zn-DHBQ** resulted in a longer activation process and a similar insufficient time for mass transfer, which together with the particle size led to a higher capacitive contribution than that of **Mn-DHBQ**. These results were consistent with the Na$^+$ diffusion coefficient (D^{Na^+}), determined by the galvanostatic intermittent titration technique (GITT) (Fig. 4c). **Ni-DHBQ** showed a high Na$^+$ diffusion coefficient (D^{Na^+}), in the level of 10^{-10} cm^2 s^{-1} as shown in
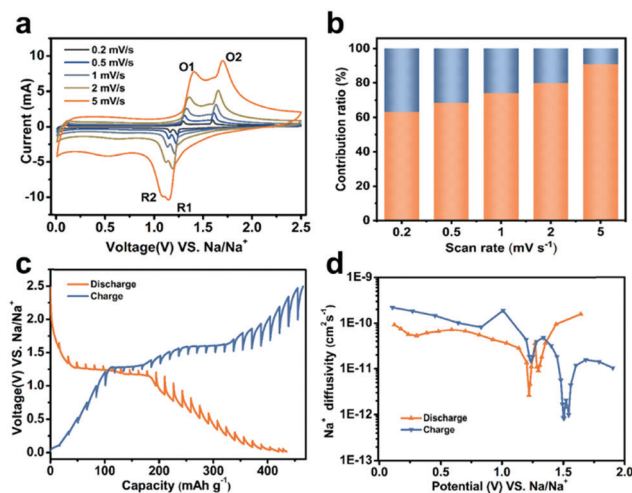

Fig. 4 (a) CV curves of the **Ni-DHBQ** electrode at different scan rates. (b) Contribution ratio of diffusion- (blue) and capacitive-controlled (orange) capacities at different scan rates for **Ni-DHBQ**. (c) GITT potential response curve with time. (d) The plot of Na-ion diffusivity calculated from GITT methods *versus* potential.

This journal is © The Royal Society of Chemistry 2022

J. Mater. Chem. C, 2022, **10**, 2592–2599 | **2595**

Fig. 4d. On the other hand, the Na-ion diffusivity of **Zn-DHBQ** was lower than that of the **Mn-DHBQ** electrode, although the grain size of **Mn-DHBQ** was larger than that of **Zn-DHBQ** (Fig. S17 and S18, ESI‡), which should be also ascribed to the higher crystallinity of **Zn-DHBQ** and was in good agreement with the above-mentioned results. The sluggish Na-ion diffusion was observed at the cathodic and anodic peak, corresponding to the intercalation process in the redox reaction.

Charge storage mechanism of M-DHBQ

To gain more insights into the redox mechanism, *ex situ* FT-IR and XPS spectra of **M-DHBQ** were studied. Upon electrochemical reduction of **Ni-DHBQ**, the representative C=O vibration at 1530 cm^{-1} gradually decreased, accompanied by the appearance of two absorption peaks at 1456 and 1402 cm^{-1}, which was consistent with the C=O bond stretching in dhbq^{3-} and dhbq^{4-} moieties after reduction (Fig. 5a).[38] The C–O stretching band ($\sim$1263 cm^{-1}) underwent a blue shift with enhanced relative intensity after discharge and recovered after recharge, which related to the insertion and extraction of sodium ions, respectively. These results suggested the reduction and recovery of the C=O double bonds in the ligands and agreed well with the two-electron reaction mechanism for quinone-based electrode materials,[5,6,48,49] and could also be confirmed by the results for **Mn-DHBQ** and **Zn-DHBQ** electrodes (Fig. S19, ESI‡). Furthermore, the *ex situ* XPS analysis of **Ni-DHBQ** showed similar phenomena. As depicted in Fig. 5b, the peak intensity of C=O at $\sim$289.2 eV and C–O at $\sim$286.5 eV changed reversibly during the electrochemical reaction, which confirmed that C=O groups were involved in the redox process.[50] The O 1s spectra (Fig. S20, ESI‡) also reconfirmed this charge storage mechanism. Compared with the pristine electrodes, the signal of C–O single bonds ($\sim$531.6 eV) increased obviously with the weakening intensity of C=O double bonds ($\sim$533.0 eV), after being fully discharged. Besides, both the peaks shifted to a lower binding energy, indicating the weakening of the C–O/C=O bonds during sodium ion insertion. After recharging to 2.5 V, the relative peaks returned back to their original states. These results clearly showed the transformation from C=O double bonds to C–O single bonds. However, the *ex situ* XPS spectra of Ni 2p showed that the valence of Ni remained stable

at +2, which was consistent with our previous works. These results indicated that it was not appropriate to detect low valent Ni (Fig. S21, ESI‡) by using the *ex situ* XPS.[43] As shown in Fig. S22 (ESI‡), the XPS spectra of Mn 2p and Zn 2p also displayed negligible change after discharge and full charge, indicating the unchanged valence of Mn^{2+} and Zn^{2+} during cycling.[51] However, the above analysis indicated that the three materials should be different and Ni should be reduced to a monovalent state after being fully discharged.

The evolution of free electrons during charging/discharging was hence monitored by EPR spectra. Although we have proposed that the ideal CCPs should be electroneutral and electron delocalized, and contain radicals,[31] the pristine samples of **M-DHBQ** showed silent EPR signals, indicating the absence of uncoupled ligand-centred free radicals (Fig. 5c and Fig. S23, ESI‡). These results should be ascribed to the precursor, *i.e.* the free ligand 2,5-dihydroxy-1,4-benzoquinone, which was already in the oxidized state. In this case, the obtained pristine CCPs were not as delocalized as the ideal structures. When the electrodes were discharged to 1.6 V, a sharp EPR signal centred at *g* = 2.002 appeared, which could be ascribed to the presence of an unpaired electron on the ligands after obtaining one electron per coordination unit. When the electrodes were discharged to 1.0 V, the almost disappeared EPR signal indicated the two-electron transfer per coordination unit (Fig, S24, ESI‡). When they were further discharged to 0.5 V, the EPR signal appeared again and increased at 0.01 V, for **Ni-DHBQ**; on the other hand, **Zn-DHBQ** electrodes showed negligible EPR signals after full discharge. The re-appearing EPR signal of the **Ni-DHBQ** electrode at low voltages should be related to the valence change of Ni to low valence.[16,31,43] Moreover, the recharged samples of all of them exhibited obvious EPR signals, which suggested that the charge/discharge process induced the rearrangement of electrons and resulted in electron delocalization of the whole CCPs, approaching the ideal structures of CCPs after redox activation.[31]

Stabilization of the cycling performance of Ni-DHBQ

These results indicated that the **Ni-DHBQ** electrodes involved three electron transfer with C=O bonds and Ni(ɪɪ) reduced to
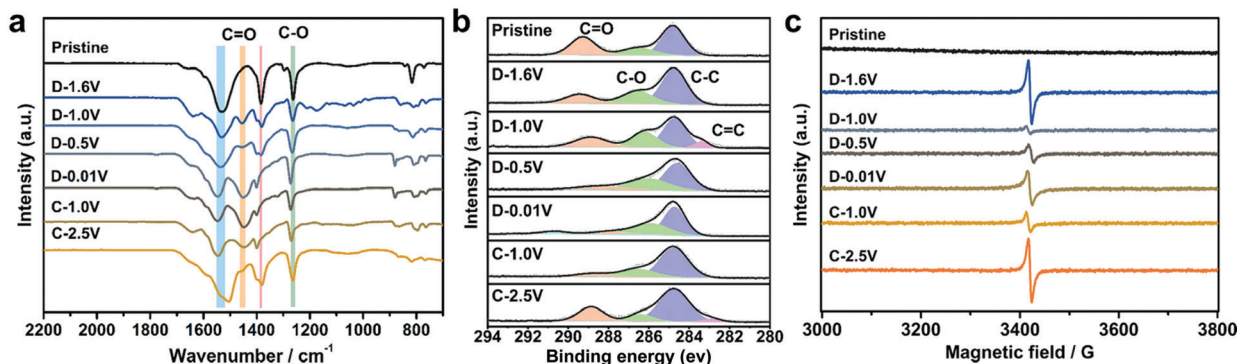

Fig. 5 *Ex situ* (a) FT-IR spectra, (b) XPS C 1s spectra and (c) EPR spectra of the **Ni-DHBQ** electrode recorded at different potentials.

2596 | *J. Mater. Chem. C*, 2022, **10**, 2592–2599

This journal is © The Royal Society of Chemistry 2022

C–O bonds and Ni(I), respectively after discharging. On the other hand, **Zn-DHBQ** and **Mn-DHBQ** electrodes involved only two electron transfer with C=O bonds reduced to C–O bonds after discharging. This different mechanism contributed to the different electrochemical performance, *i.e.* higher capacity but poorer cyclability of **Ni-DHBQ** electrodes compared with **Zn-DHBQ** and **Mn-DHBQ**. The reduction of metal ions may result in the weakening of M–O bonds and therefore lead to poor structural stability, which caused the relatively low CE and capacity decay.[22,25] However, it should be noted that the capacity decay mostly occurred in the initial cycles (Fig. 3c and e). The *ex situ* PXRD patterns and SEM images of **Ni-DHBQ** electrodes were hence recorded at different potentials to detect the reason for the capacity decay of **Ni-DHBQ**. As shown in Fig. S25 (ESI‡), the peaks at $2\theta = 12.16$ (001) and 18.13° (110) showed a slight shift to lower angles when being discharged to 1.0 V, indicating that the insertion of Na$^+$ ions into **Ni-DHBQ** resulted in the increase of the lattice constant. However, further embedding of Na$^+$ ions increased the interactions between the skeletons by the Na$^+$ ions, causing the shrinking of the unit cell, after being discharged to 0.01 V,[20] although the intensity became weak. When the **Ni-DHBQ** electrode was fully charged, the lattice parameters returned to the initial states, indicating the reversibility of **Ni-DHBQ**. The morphologies of **Ni-DHBQ** after cycling were further investigated by SEM. As shown in Fig. 6, after being discharged to low voltages (*e.g.* 0.5 V), the particle size of **Ni-DHBQ** became very small, which was pulverized after being further discharged to 0.01 V. This should be the reason that **Ni-DHBQ** showed weakened XRD intensity after being discharged to 0.01 V.[52] Although the morphologies of the **Ni-DHBQ** electrode recovered after it was recharged to 2.5 V, the reduction of particle size was observed after long-term cycling. The morphological variation may result in the irreversible capacity contribution and hence lead to poor cyclability, particularly in the first cycles. On the other hand, the morphologies of **Zn-DHBQ** showed negligible change after cycling (Fig. S26, ESI‡).

We therefore narrowed the working potential range of **Ni-DHBQ** to 0.5–2.3 V (*vs.* Na/Na$^+$). As shown in Fig. S27 (ESI‡), the particle size of the **Ni-DHBQ** electrode was stable in this voltage range. In this electrochemical window, the two distinct redox peaks in the range of 1.4–1.7 V remained. Moreover, the
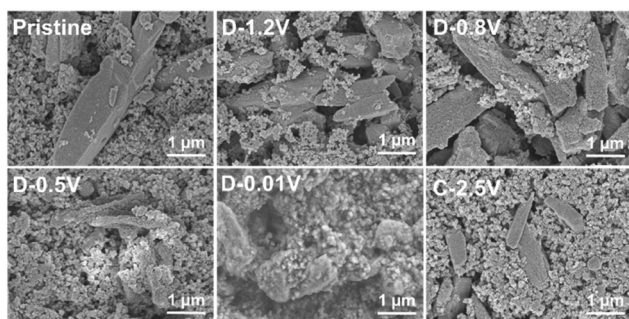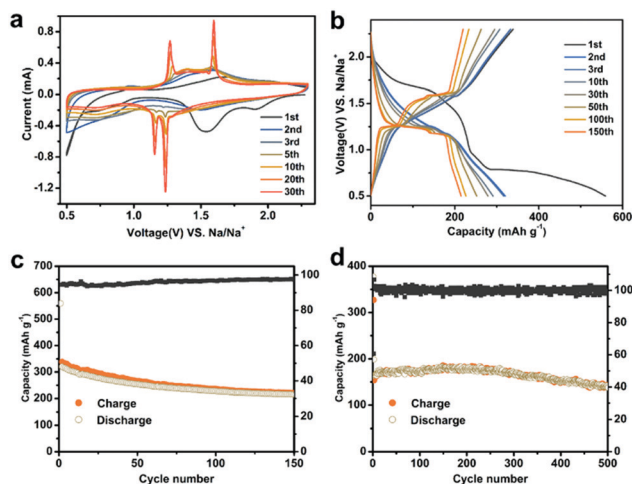

Fig. 7 Electrochemical performance of the **Ni-DHBQ** electrode recorded in the voltage range of 0.5–2.3 V (*vs.* Na/Na$^+$). (a) CV curves at a scan rate of 0.5 mV s^{-1}. (b) Discharge–charge voltage profiles of **Ni-DHBQ** electrodes at 0.1 A g^{-1}. (c) and (d) Cycling performance of **Ni-DHBQ** electrodes at a current density of 0.1 A g^{-1} and 5 A g^{-1}, respectively.

peak at about 0.72 V could still be observed after 30 cycles (Fig. 7a), showing higher stability than that in the voltage range of 0.01–2.5 V. As a result, at 100 mA g^{-1} in the 0.5–2.3 V range, the capacity reached ~320 mA h g^{-1}, and ~215 mA h g^{-1} was retained after 150 cycles (Fig. 7b and c), with a capacity retention of 67% (compared with 57% in the 0.01–2.5 V range). In this electrochemical window, the **Ni-DHBQ** electrode still delivered a discharge capacity of 346, 312, 294, 266, 241, and 215 mA h g^{-1} at current densities of 50, 100, 200, 500, 1000, and 2000 mA g^{-1}, respectively (Fig. S28, ESI‡). At a current density of 1 A g^{-1}, a capacity of about ~200 mA h g^{-1} could be achieved after 200 cycles with a capacity retention of 71% (compared with 58% in the 0.01–2.5 V range, Fig. S29, ESI‡). Moreover, the **Ni-DHBQ** electrode still delivered a capacity of 140 mA h g^{-1} after 500 cycles with a capacity retention of 78% even at a current density of 5 A g^{-1}, revealing it to be more stable than other DHBQ based electrodes (Table S1, ESI‡).[41,42,53–56]

Conclusion

In conclusion, DHBQ was selected to construct one dimensional conjugated coordination polymers with different metal nodes (**M-DHBQ**) for SIBs. Comprehensive characterizations revealed that the sodium storage of **Mn-** and **Zn-DHBQ** involved the redox reactions of only ligands, while **Ni-DHBQ** involved the redox reactions of both ligands and non-innocent Ni^{2+} ions. Benefiting from the redox active quinone groups as well as metal ions, **Ni-DHBQ** delivered a high reversible capacity of around 321.2 mA h g^{-1} at 0.1 A g^{-1} after 150 cycles and superior rate performance (~267 mA h g^{-1} at 2 A g^{-1}). Additionally, the voltage window was adjusted for **Ni-DHBQ** to suppress the morphological variation during cycling, leading to enhanced cyclability and capacity retention. These results highlighted the importance of the rational choice of metal ions for high

Fig. 6 SEM image of the **Ni-DHBQ** electrode recorded at different potentials.

capacity and cycle stability, and deepen our understanding on CCPs for further designing high performance SIBs.

Experimental section

Materials and physical measurements

All starting materials were of reagent grade quality and were obtained from commercial sources without further purification. Scanning electron microscopy (SEM) images were recorded on a ZEISS Gemini 300 electron microscope. Powder X-ray diffraction (PXRD) patterns were recorded on an X'Pert3 Powder instrument with Cu Kα X-ray radiation at room temperature. Infrared spectra were measured as KBr pellets on a Bruker ALPHA spectrometer in the range of 400–4000 cm^{-1}. Thermogravimetric analyses (TGA) were performed under a flow of nitrogen in the temperature range 25–600 °C at a heating rate of 5 °C per min using a Pyris1 thermogravimetric analyzer. The XPS spectrum was collected on a Thermo Fisher Esca Lab 250Xi using a monochromic Al X-ray source (hv = 1486.6 eV). Elemental analyses for C, H and N were obtained with a Vario Micro Cube Elemental Analyzer. X-Band EPR spectra were acquired on a Bruker EMS nano spectrometer at room temperature.

Synthesis of M(DHBQ)(H$_2$O)$_2$ (M = Ni, Mn and Zn)

Ni(OAc)$_2$·4H$_2$O (2.48 g, 10 mmol) was dissolved in 50 mL of distilled water. Then DHBQ (10 mmol, 1.4 g) in 450 mL of H$_2$O was added dropwise over 15 min. The mixture was left to reflux for an additional 30 min. A gray precipitate was obtained by vacuum filtration and washed with water. Yield: 1.86 g, 80%. Anal. calcd for NiC$_6$H$_6$O$_6$: C, 30.95%; H, 2.60%; O, 41.23%; found: C, 31.35%; H, 2.08%; O, 41.76%. IR data (KBr, cm^{-1}): 3340 (m), 2931 (w), 1672 (w), 1533 (s), 1384 (s), 1296 (w), 1263 (s), 842 (w), 817 (s), 773 (w), 535 (m), 476 (w), 416 (w).

Mn(DHBQ)(H$_2$O)$_2$ and **Zn(DHBQ)(H$_2$O)$_2$** were synthesized by a similar method, except that the metal salt was replaced by MnSO$_4$·5H$_2$O or ZnSO$_4$·7H$_2$O. The red powder of **Mn(DHBQ)(H$_2$O)$_2$** was filtered off and washed with water. Yield: 1.79 g, 78%. Anal. calcd for MnC$_6$H$_6$O$_6$: C, 31.46%; H, 2.64%; found: C, 30.81%; H, 1.89%. IR data (KBr, cm^{-1}): 3328 (m), 2937 (w), 1643 (w), 1612 (w), 1539 (s), 1396 (m), 1375 (s), 1296 (w), 1249 (s), 838 (w), 829 (m), 817 (m), 769 (m), 559 (w), 505 (m).

The purple precipitate of **Zn(DHBQ)(H$_2$O)$_2$** was obtained by vacuum filtration and was washed with water. Yield: 1.77 g, 74%. Anal. calcd for ZnC$_6$H$_6$O$_6$: C, 30.09%; H, 2.52%; found: C, 30.24%; H, 2.39%. IR data (KBr, cm^{-1}): 3351 (m), 2942 (w), 1650 (w), 1602 (w), 1537 (s), 1382 (s), 1297 (w), 1265 (s), 838 (w), 821 (s), 798 (w), 769 (w), 748 (w), 524 (m), 484 (w), 458 (w).

Electrochemistry

Before the electrochemical study, each sample was dried at 60 °C under vacuum for 12 h. The working electrodes for SIBs were prepared by mixing the as-prepared active materials **M-DHBQ**, super P carbon black, and polyvinylidene fluoride (PVDF) at a weight ratio of 6 : 3 : 1, using *N*-methyl-2-pyrrolidone

(NMP) as a homogenizer. Then the slurry was coated onto Cu foil using a doctor blade and dried for 12 h in vacuum at 60 °C. A disc of sodium (diameter of 14.0 mm) was used as the counter electrode and a glass fiber membrane (Whatman, GF/B) with a diameter of 19.0 mm was used as a separator. Finally, the 2032 coin-type cells assembly was carried out in an Ar-filled glovebox with O$_2$ and H$_2$O levels below 0.1 ppm. 1 M NaPF$_6$ dissolved in dimethyl ether (DME) was used as the electrolyte. The half-cells were galvanostatically cycled in different voltage ranges on the LANHE-CT2001A test system (Wuhan, China) at room temperature. Cyclic voltammetry (CV) was performed by using a BioLogic VMP3 potentiostat in different voltage ranges at scan rates of 0.2, 0.5, 1, 2, and 5 mV s^{-1}. For *ex situ* experiments, the battery cells were first cycled to the desired state of charge at a current density of 100 mA g^{-1} and then disassembled in an argon-filled glove box with oxygen and water levels less than 0.1 ppm.

Conflicts of interest

There are no conflicts to declare.

Acknowledgements

Notes and references

1 Y. W. Wu, R. H. Zeng, J. M. Nan, D. Shu, Y. C. Qiu and S. L. Chou, *Adv. Energy Mater.*, 2017, **7**, 1700278.

2 M. Tang, H. Li, E. Wang and C. Wang, *Chin. Chem. Lett.*, 2018, **29**, 232–244.

3 L. M. Zhu, G. C. Ding, L. L. Xie, X. Y. Cao, J. P. Liu, X. F. Lei and J. X. Ma, *Chem. Mater.*, 2019, **31**, 8582–8612.

4 T. B. Schon, B. T. McAllister, P. F. Li and D. S. Seferos, *Chem. Soc. Rev.*, 2016, **45**, 6345–6404.

5 Y. Chen, S. M. Zhuo, Z. Y. Li and C. L. Wang, *EnergyChem*, 2020, **2**, 100030.

6 Y. Chen and C. Wang, *Acc. Chem. Res.*, 2020, **53**, 2636–2647.

7 J. Calbo, M. J. Golomb and A. Walsh, *J. Mater. Chem. A*, 2019, **7**, 16571–16597.

8 W.-H. Li, W.-H. Deng, G.-E. Wang and G. Xu, *EnergyChem*, 2020, **2**, 100029.

9 J. Liu, D. Xie, W. Shi and P. Cheng, *Chem. Soc. Rev.*, 2020, **49**, 1624–1642.

10 K. Sakaushi and H. Nishihara, *Acc. Chem. Res.*, 2021, **54**, 3003–3015.

2598 | *J. Mater. Chem. C*, 2022, **10**, 2592–2599

This journal is © The Royal Society of Chemistry 2022

11 L. S. Xie, G. Skorupskii and M. Dinca, *Chem. Rev.*, 2020, **120**, 8536–8580.

12 M. Yu, R. Dong and X. Feng, *J. Am. Chem. Soc.*, 2020, **142**, 12903–12915.

13 M. Wang, R. Dong and X. Feng, *Chem. Soc. Rev.*, 2021, **50**, 2764–2793.

14 X. Huang, P. Sheng, Z. Tu, F. Zhang, J. Wang, H. Geng, Y. Zou, C. A. Di, Y. Yi, Y. Sun, W. Xu and D. Zhu, *Nat. Commun.*, 2015, **6**, 7408.

15 X. Huang, S. Zhang, L. Liu, L. Yu, G. Chen, W. Xu and D. Zhu, *Angew. Chem., Int. Ed.*, 2018, **57**, 146–150.

16 C. Y. Zhang, K. Fan, Y. Chen, Y. C. Wu and C. L. Wang, *ACS Appl. Electron. Mater.*, 2021, **3**, 1947–1958.

17 J. Liu, X. Song, T. Zhang, S. Liu, H. Wen and L. Chen, *Angew. Chem., Int. Ed.*, 2021, **60**, 5612–5624.

18 Z. Wu, D. Adekoya, X. Huang, M. J. Kiefel, J. Xie, W. Xu, Q. Zhang, D. Zhu and S. Zhang, *ACS Nano*, 2020, **14**, 12016–12026.

19 Y. Wu, Y. Chen, M. Tang, S. Zhu, C. Jiang, S. Zhuo and C. Wang, *Chem. Commun.*, 2019, **55**, 10856–10859.

20 Y. Chen, Q. Zhu, K. Fan, Y. Gu, M. Sun, Z. Li, C. Zhang, Y. Wu, Q. Wang, S. Xu, J. Ma, C. Wang and W. Hu, *Angew. Chem., Int. Ed.*, 2021, **60**, 18769.

21 M. Majumder, M. S. Santosh, R. Viswanatha, A. K. Thakur, D. P. Dubal and K. Jayaramulu, *Energy Storage Mater.*, 2021, **37**, 396–416.

22 J. Park, M. Lee, D. Feng, Z. Huang, A. C. Hinckley, A. Yakovenko, X. Zou, Y. Cui and Z. Bao, *J. Am. Chem. Soc.*, 2018, **140**, 10315–10323.

23 L. Wang, Y. Ni, X. Hou, L. Chen, F. Li and J. Chen, *Angew. Chem., Int. Ed.*, 2020, **59**, 22126–22131.

24 J. Xie, X. F. Cheng, X. Cao, J. H. He, W. Guo, D. S. Li, Z. J. Xu, Y. Huang, J. M. Lu and Q. Zhang, *Small*, 2019, **15**, 1903188.

25 Q. Jiang, P. Xiong, J. Liu, Z. Xie, Q. Wang, X. Q. Yang, E. Hu, Y. Cao, J. Sun, Y. Xu and L. Chen, *Angew. Chem., Int. Ed.*, 2020, **59**, 5273–5277.

26 A. Nazir, H. T. T. Le, C. W. Min, A. Kasbe, J. Kim, C. S. Jin and C. J. Park, *Nanoscale*, 2020, **12**, 1629–1642.

27 K. Wada, H. Maeda, T. Tsuji, K. Sakaushi, S. Sasaki and H. Nishihara, *Inorg. Chem.*, 2020, **59**, 10604–10610.

28 X. Wu, Y. Qiu, Z. Chen, B. Guan, X. Hao, A. I. Rykov, Y. Sun, L. Liu, Y. Zou, J. Sun, W. Xu and D. Zhu, *Angew. Chem., Int. Ed.*, 2020, **59**, 20873–20878.

29 A. C. Hinckley, J. Park, J. Gomes, E. Carlson and Z. Bao, *J. Am. Chem. Soc.*, 2020, **142**, 11123–11130.

30 Z. Wang, G. Wang, H. Qi, M. Wang, M. Wang, S. Park, H. Wang, M. Yu, U. Kaiser, A. Fery, S. Zhou, R. Dong and X. Feng, *Chem. Sci.*, 2020, **11**, 7665–7671.

31 K. Fan, C. Y. Zhang, Y. Chen, Y. C. Wu and C. L. Wang, *Chem*, 2021, **7**, 1224–1243.

32 S. Kitagawa and S. Kawata, *Coord. Chem. Rev.*, 2002, **224**, 11–34.

33 S. Morikawa, T. Yamada and H. Kitagawa, *Chem. Lett.*, 2009, **38**, 654–655.

34 T. Yamada, S. Morikawa and H. Kitagawa, *Bull. Chem. Soc. Jpn.*, 2010, **83**, 42–48.

35 K. V. Nielson, L. Zhang, Q. Zhang and T. L. Liu, *Inorg. Chem.*, 2019, **58**, 10756–10760.

36 J. Montero, D. Arenas-Esteban, D. Ávila-Brande, E. Castillo-Martínez, S. Licoccia and J. Carretero-González, *Electrochim. Acta*, 2020, **341**, 136063.

37 J. Tao, H. Maruyama and O. Sato, *J. Am. Chem. Soc.*, 2006, **128**, 1790–1791.

38 M. E. Ziebel, L. E. Darago and J. R. Long, *J. Am. Chem. Soc.*, 2018, **140**, 3040–3051.

39 K. Kon, K. Uchida, K. Fuku, S. Yamanaka, B. Wu, D. Yamazui, H. Iguchi, H. Kobayashi, Y. Gambe, I. Honma and S. Takaishi, *ACS Appl. Mater. Interfaces*, 2021, **13**, 38188–38193.

40 X.-F. Cheng, E.-B. Shi, X. Hou, J. Shu, J.-H. He, H. Li, Q.-F. Xu, N.-J. Li, D.-Y. Chen and J.-M. Lu, *Adv. Electron. Mater.*, 2017, **3**, 1700107.

41 C. Luo, J. J. Wang, X. L. Fan, Y. J. Zhu, F. D. Han, L. M. Suo and C. S. Wang, *Nano Energy*, 2015, **13**, 537–545.

42 Z. Zhu, H. Li, J. Liang, Z. Tao and J. Chen, *Chem. Commun.*, 2015, **51**, 1446–1448.

43 Y. Chen, M. Tang, Y. Wu, X. Su, X. Li, S. Xu, S. Zhuo, J. Ma, D. Yuan and C. Wang, *Angew. Chem., Int. Ed.*, 2019, **58**, 14731–14739.

44 H. N. He, D. Sun, Y. G. Tang, H. Y. Wang and M. H. Shao, *Energy Storage Mater.*, 2019, **23**, 233–251.

45 F. Zou, Y. M. Chen, K. Liu, Z. Yu, W. Liang, S. M. Bhaway, M. Gao and Y. Zhu, *ACS Nano*, 2016, **10**, 377–386.

46 Z.-Q. Lin, J. Xie, B.-W. Zhang, J.-W. Li, J. Weng, R.-B. Song, X. Huang, H. Zhang, H. Li, Y. Liu, Z. J. Xu, W. Huang and Q. Zhang, *Nano Energy*, 2017, **41**, 117–127.

47 S. Zhuo, M. Tang, Y. Wu, Y. Chen, S. Zhu, Q. Wang, C. Xia and C. Wang, *Nanoscale Horiz.*, 2019, **4**, 1092–1098.

48 C. L. Wang, *Energy Environ. Mater.*, 2020, **3**, 441–452.

49 M. Tang, S. Zhu, Z. Liu, C. Jiang, Y. Wu, H. Li, B. Wang, E. Wang, J. Ma and C. Wang, *Chem*, 2018, **4**, 2600–2614.

50 H. J. Kim, Y. Kim, J. Shim, K. H. Jung, M. S. Jung, H. Kim, J. C. Lee and K. T. Lee, *ACS Appl. Mater. Interfaces*, 2018, **10**, 3479–3486.

51 Y. J. Liu, X. L. Zhao, C. Fang, Z. Ye, Y. B. He, D. N. Lei, J. Yang, Y. Zhang, Y. Y. Li, Q. Liu, Y. Huang, R. Zeng, L. T. Kang, J. J. Liu and Y. H. Huang, *Chem*, 2018, **4**, 2463–2478.

52 Y. C. Wu, S. M. Zhuo, M. Tang, Y. Chen, B. Wang, S. L. Zhu, K. Fan, C. Jiang and C. L. Wang, *J. Power Sources*, 2020, **478**, 228778.

53 X. Wu, S. Jin, Z. Zhang, L. Jiang, L. Mu, Y. S. Hu, H. Li, X. Chen, M. Armand, L. Chen and X. Huang, *Sci. Adv.*, 2015, **1**, e1500330.

54 X. Wu, J. Ma, Q. Ma, S. Xu, Y.-S. Hu, Y. Sun, H. Li, L. Chen and X. Huang, *J. Mater. Chem. A*, 2015, **3**, 13193–13197.

55 D. Wu, Y. Huang and X. Hu, *Chem. Commun.*, 2016, **52**, 11207–11210.

56 A. Li, Z. Feng, Y. Sun, L. Shang and L. Xu, *J. Power Sources*, 2017, **343**, 424–430.

This journal is © The Royal Society of Chemistry 2022

J. Mater. Chem. C, 2022, **10**, 2592–2599 | **2599**